Nanoscale

ROYAL SOCIETY
OF CHEMISTRY

PAPER

Check for updates

Piezoelectrically enhanced photocatalysis of $K_xNa_{1-x}NbO_3$ (KNN) microstructures for efficient water purification†

Runjiang Guo,‡[a] Mengqian Liu,‡[a] Yurui Xing,[a] Tanglong Bai,[a] Chenglong Zhao,[a] Haolin Huang[a] and Hongti Zhang [iD] *[a,b]

As a kind of excellent multifunctional metal oxide semiconductor, $K_xNa_{1-x}NbO_3$ (KNN) has been widely applied in a variety of fields such as photocatalysis and energy harvesting due to its excellent piezoelectric, dielectric and photovoltaic properties in recent decades. In this report, octahedron-shaped $K_{0.4}Na_{0.6}NbO_3$ (KNN-6) microstructures assembled by cubic nanoparticles with {010} exposed facets were synthesized *via* a one-pot hydrothermal reaction. Due to the accumulation of electrons on the exposed facets, which was conducive to the separation of photo-generated electron–hole pairs, the microstructures could achieve a highly efficient photocatalytic performance for wastewater degradation. In addition, owing to the piezoelectric effect of KNN crystals, the degradation efficiency could be further enhanced by introducing ultrasonic vibration. Using methylene blue (MB) as the organic dye to evaluate their wastewater degradation efficiency, the KNN microstructures achieved their best catalytic performance when the atomic ratio of KOH to NaOH in the reactant was set at 4 : 6 (KNN-6). Under the synergistic effect of light irradiation and ultrasonic vibration, MB could almost be completely (99%) degraded within 40 minutes by KNN-6 microstructures, which was several times more efficient than that of pure $NaNbO_3$ or $KNbO_3$ in previous reports. This work demonstrated that the $K_{0.4}Na_{0.6}NbO_3$ (KNN-6) microstructure could be a prominent candidate for wastewater purification. The formation mechanism of KNN crystals and the role of the piezoelectric effect in the photocatalytic process were also discussed.

Introduction

Photocatalysis is a powerful technology for wastewater treatment, which can completely degrade organic dyes or other pollutants without causing secondary pollution.[1–5] However, in the case of traditional photocatalysts, their low light utilization efficiencies and high electron–hole recombination rates limit their further applications in the photocatalysis field. Therefore, the fabrication of highly efficient photocatalysts has become a hotspot in the field of environmental protection.

In recent years, researchers found that photocatalytic performance could be improved by ferroelectric polarization and piezo-photoelectronic effects. This coupling effect between the piezoelectric effect and photoresponsiveness was first discov-

[a]*School of Physical Science and Technology, ShanghaiTech University, Shanghai, 201210, P. R. China. E-mail: zhanght3@shanghaitech.edu.cn*
[b]*Shanghai Key Laboratory of High-resolution Electron Microscopy, ShanghaiTech University, Shanghai, 201210, P. R. China*
†Electronic supplementary information (ESI) available. See DOI: https://doi.org/10.1039/d2nr07311k
‡These authors contributed equally to this work.

ered in ZnO nanowires by Wang *et al.*[6] As shown in that report, by using the piezoelectric field to hinder the recombination of photogenerated electrons and holes, the combined piezoelectric effect and photoresponsiveness could effectively enhance the photocatalytic performance, which was also widely applied in photovoltaic devices or PECs.[7] In addition, the separation of photo-generated electrons and holes would generate an internal electric field, which can lead to the in turn switching of polarization. This intriguing phenomenon also attracts vast attention in the environmental protection field.[8]

Some piezoelectric semiconductors, such as CdS, $ZnSnO_3$, $BaTiO_3$, $PbZr_{1-x}Ti_xO_3$ (PZT), ZnO, ZIF-8, $CoFe_2O_4$, $NiCo_2O_4$, BiOCl, g-C_3N_4 and $Bi_xNa_{1-x}TiO_3$-$BaTiO_3$(NBBT), are often used as piezo-photocatalysts in applications such as wastewater purification and water splitting.[9–23] For instance, using CdS as the piezo-photocatalyst for the photocatalytic production of H_2, Zhao *et al.* achieved a high hydrogen yield rate reaching ~20 μL h^{-1} with an optimized coupling of piezoelectric field and photocatalysis.[9] Wang *et al.* synthesized a kind of $ZnSnO_3$ nanowires that can degrade more than 92% of rhodamine (RhB) within 60 min by synergistically applying ultrasonic vibration and light irradiation, which was 1.53 and 2.3 times

more effective than applying them separately.[10] However, among all the piezoelectric metal–oxide semiconductors, niobates, especially potassium niobate ($KNbO_3$) and sodium niobate ($NaNbO_3$), have the potential of being prominent piezo-photocatalysts due to their high carrier mobility and outstanding chemical stabilities.[24–26] A chemically stable $NaNbO_3$ semiconductor designed by Singh *et al.* could degrade about 78% of MB within 180 min under the combined effect of irradiation and vibration, which was much higher than that of ZnO, demonstrating that niobates might have a great potential in the field of piezo-photocatalysis.[27] Apart from $NaNbO_3$, niobate $KNbO_3$ was also applied in the field of piezo-photocatalysis. As reported by Yu *et al.*, a sheet-like $KNbO_3$ catalyst with the (010) exposed facet alongside one of the polarization components could degrade about 92.6% RhB solution in 120 min under external vibration, with the photocurrent density increased by 55%.[28] Due to their non-centrosymmetric structures, niobates also had pyroelectric properties. Jia *et al.* synthesized $NaNbO_3$ nanofibers *via* the hydrothermal reaction, which could degrade more than 86% RhB in 80 min under both ultrasonic vibration and 15–50 °C cold–hot cycles without any light irradiation.[29]

Recently, researchers have found that antiferroelectric-type $NaNbO_3$ could be dissolved into ferroelectric-type $KNbO_3$ to form a single-phase solid solution $K_{1-x}Na_xNbO_3$ (KNN).[30,31] Better piezoelectric properties of KNN materials were demonstrated by Saito *et al.*[32] who prepared hexa-membered ceramics with piezoelectric constants as high as 416 pC/N, which was comparable to the conventional lead-containing piezoelectric material $PbZr_xTi_{1-x}O_3$. Therefore, KNN materials might have a better piezo-photocatalytic performance than pure $NaNbO_3$ or $KNbO_3$. Although the KNN samples have been used in many fields such as supercapacitors, energy harvesters, and solar cells,[33–37] there were only a few reports about their potential as piezoelectrically enhanced photocatalysts for wastewater treatment (as shown in the ESI†).

Hongti Zhang

Dr. Hongti Zhang is currently an Assistant Professor in the School of Physical Science and Technology at ShanghaiTech University. He obtained his Ph.D. degree in Mechanical Engineering from City University of Hong Kong in 2016 and worked there as a postdoctoral researcher before joining ShanghaiTech University in November 2018. His research interests focus on investigating the mechanical properties of functional nanomaterials and exploring their strain-induced property changes (elastic strain engineering) via in situ electron microscopy techniques.

In this study, a series of KNN microstructures with different K and Na contents were prepared through hydrothermal reactions, and their methylene blue (MB) catalytic degradation efficiencies were evaluated under conditions of light irradiation, ultrasonic vibration, and their synergistic effect. From the results, we found that the KNN samples with the K : Na atomic ratio of 4 : 6 (*i.e.*, KNN-6) exhibited the best degradation efficiency, which could almost completely degrade the MB solution within 40 minutes under the synergistic effect of light irradiation and ultrasonic vibration, which was several times faster than the previously reported pure $NaNbO_3$, $KNbO_3$, and other types of metal–oxide semiconductor photocatalysts.[27,38,39] This work showed the possibility of using low-cost niobate microstructures as effective photocatalysts for wastewater purification and discussed the auxiliary mechanism of piezoelectricity in photocatalysis.

Experimental section

Material synthesis

Material preparation. Potassium hydroxide (KOH, ≥96%), sodium hydroxide (NaOH, ≥96%) and methylene blue (MB) were purchased from Collins. Niobium(ᴠ) oxide (Nb_2O_5, ≥99%) and *p*-benzoquinone (BQ) were purchased from Sinopharm Chemical Reagent Co., Ltd. Terephthalic acid (TA) was purchased from Sangon Biotech (Shanghai) Co., Ltd. Nitrotetrazolium blue chloride (NBT) was purchased from Meilun Biotechnology Co., Ltd. *tert*-Butanol (TBA) and edetate disodium dihydrate (EDTA-2Na) were purchased from Shanghai Titan Scientific Co., Ltd.

Synthesis of $K_xNa_{1-x}NbO_3$ (KNN)

The KNN powder was synthesized *via* a hydrothermal reaction. In a typical process, specific amounts of NaOH and KOH were dissolved in deionized (DI) water to form an alkaline solution with the concentration of OH- being 10 M. Then, 0.3 g of Nb_2O_5 was dispersed in the as-prepared alkaline solution under continuous stirring. We transferred the resulting suspension into a Teflon-lined stainless-steel autoclave and held it at 200 °C for 24 h. After the reaction, we washed the final product with DI water and C_2H_5OH several times to remove the remaining impurities. Afterwards, the product was dried at 80 °C for 5 h, and then the white KNN samples were finally obtained.

In order to obtain KNN powders with different Na/K ratios, we changed the concentration of NaOH and KOH in the reactant, and labeled KNN powders with different Na/K ratios as KNN-0 to KNN-10, as provided in Table 1. From KNN-0 to KNN-10, the concentration of the K element in KNN increased gradually.

In order to investigate the formation mechanism of KNN microstructures, we changed the temperatures (180 °C, 190 °C and 200 °C for 24 h) and durations (1, 2, 4, 8, 16 and 24 h at 200 °C) of the hydrothermal reactions to monitor their growth procedures.

Table 1 KNN powders with different Na/K ratios

Sample no.	KNN-0	KNN-5	KNN-6	KNN-7	KNN-8	KNN-9	KNN-10
KOH concentration (mol L^{-1})	0	5	6	7	8	9	10
NaOH concentration (mol L^{-1})	10	5	4	3	2	1	0
Total concentration (mol L^{-1})	10	10	10	10	10	10	10

Material characterization

The morphologies of the as-prepared KNN powders were investigated using a scanning electron microscope (SEM, JEOL JSM-IT500HR) and a transmission electron microscope (TEM, JEOL 2100Plus) operated at accelerating voltages of 10 and 200 kV, respectively. The general phase structures were investigated by X-ray diffraction (XRD, D2 Advance, Bruker™) using Cu Kα energy as the radiation source. The elemental compositions were established by X-ray photoelectron spectroscopy (XPS, ESCALAB 250Xi, Thermo Fisher Scientific). The photoluminescence spectra were recorded using a photoluminescence spectrometer (Fluorolog-3, Horiba Scientific) using the 315 nm excitation light. Ultraviolet-visible (UV-vis) spectra were used to calculate the band gaps of KNN powders and evaluate their MB degradation efficiencies, which were recorded on a Cary 5000 spectrophotometer (Agilent Technologies). The ferroelectric properties of the KNN samples were investigated by piezoresponse force microscopy (PFM mfp-3d Asylum Research).

Photocatalytic efficiency evaluation

Methylene blue (MB) was used to evaluate the piezo-photocatalytic performance of the as-prepared KNN samples. First, we dispersed 0.1 g of the catalysts (KNN samples, KNN-0 to KNN-10) in 50 mL of MB aqueous solution at a concentration of 10 mg L^{-1}. Then, we put the suspension into an ultrasonic cleaner machine (120 W) in a dark environment for 20 minutes to reach a photo-equilibrated state. Finally, a Xe lamp was placed ~15 cm above the suspension surface as the light irradiation source. During the whole degradation process, we stirred the suspension every few minutes to exclude the influence of catalyst dispersion on our experiment. The MB solutions were degraded by the KNN powder under three different conditions: (i) UV light irradiation without ultrasonic vibration, (ii) dark environment with ultrasonic vibrations, and (iii) UV light irradiation together with ultrasonic vibrations. 5 mL of the suspension under degradation was collected every 5 minutes to monitor the MB concentration changes using a UV-vis spectrophotometer (the characteristic absorption peak of MB was ~660 nm). In addition, water in the ultrasonic cleansing machine will be replaced every 20 minutes to keep the reaction temperature stable during the whole degradation process. The photodegradation efficiency (η_{eff}) was determined according to the following eqn (1):

$$\eta_{eff} = \left(1 - \frac{A_t}{A_0}\right) \times 100\% \qquad (1)$$

where A_0 and A_t stand for the intensity of the MB absorption peak (~660 nm) before and after the catalytic reaction at a specific time.

Apart from MB, we also degraded NBT to further investigate the degradation mechanism of KNN-6. Since NBT can be easily degraded in the presence of oxidative free radicals O_2^-, the relative concentration of $^\cdot O_2^-$ generated by KNN-6 could be evaluated by the degradation efficiency of NBT. The whole process was the same as that mentioned before except for that MB was replaced with NBT and the characteristic absorption peak was changed to 270 nm, accordingly.

The photoluminescence spectra were obtained to detect the generated $^\cdot OH^-$ radicals. Typically, we dissolved terephthalic acid (TA) and NaOH in 50 mL of DI water to form a homogeneous solution with the concentration of TA being 0.5 mM and that of NaOH being 2 mM. Under the stimulation of irradiation and vibration, TA could react with the generated $^\cdot OH^-$ radicals to form TAOH which can be characterized using the photoluminescence spectra at 425 nm.

To further investigate which radicals played the most important role in the degradation process, we performed trapping experiments by introducing different kinds of radical quenchers. As it was known, disodium ethylenediaminetetraacetate (EDTA-2Na), benzoquinone (BQ) and *tert*-butylalcohol (TBA) can trap the h$^+$, $^\cdot O_2^-$, and $^\cdot OH^-$ radicals respectively. We added these three quenchers into the MB solution and repeated the abovementioned degradation processes. Then we measured the UV-vis absorbance of MB solutions to evaluate their degradation efficiencies in the absence of h$^+$, $^\cdot O_2^-$, or $^\cdot OH^-$.

Results and discussion

Structure and morphology of KNN

We used XRD to investigate the crystal structures of the as-synthesized KNN samples, and the results are shown in Fig. 1. The XRD peaks of the as-prepared KNN samples with different K/Na contents were all similar to the standard diffraction peaks of the KNbO$_3$ phase (JCPDS card no.32-0822),[28] with lattice parameters of a = 5.695 Å, b = 5.7213 Å and c = 3.9739 Å, indicating that the as-synthesized KNN samples were all perovskite-type niobate materials and no impurities were formed during the hydrothermal process. In addition, as shown in Fig. 1, with the increase of Na contents in KNN, the diffraction peaks of KNN would shift to higher angles due to the shrinkage of crystal lattices. Fig. 1(b) shows the XRD patterns for all the KNN samples ranging from 44° to 48°. For KNN-0 (pure NaNbO$_3$), KNN-5 (nearly no K element) and KNN-10 (pure
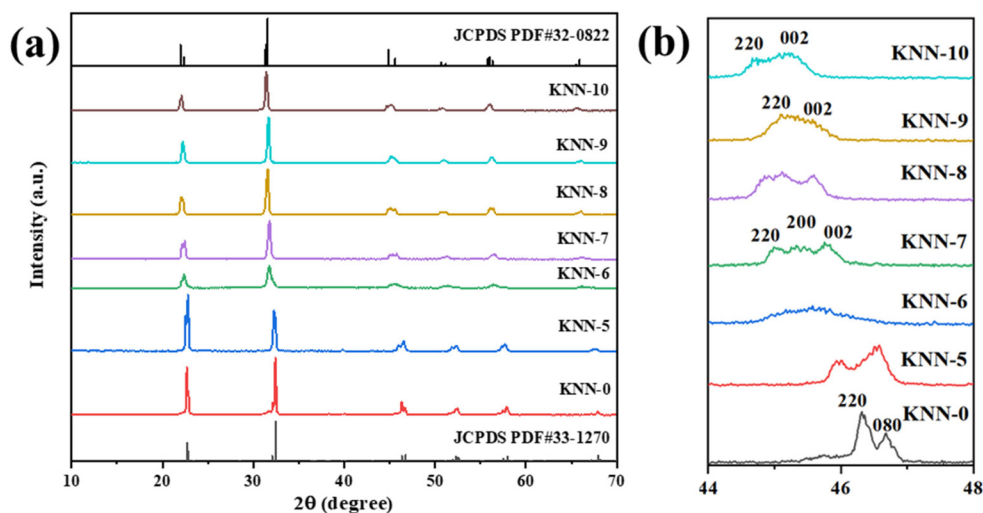
Fig. 1 The XRD patterns of the as-synthesized KNN samples with different Na/K ratios with scanning ranges of (a) 10° to 70° and (b) 44° to 48°. With the increase of the Na content, the diffraction angles shifted toward higher angles.

$KNbO_3$), the diffraction peaks were split into two peaks, which were consistent with the standard diffraction peaks for $NaNbO_3$ (JCPDS card no.33-1270, orthorhombic symmetry) and $KNbO_3$ (JCPDS card no.32-0822, orthorhombic symmetry). However, for KNN-7 to KNN-8, the diffraction peaks at 45° were split into three peaks indicating that these KNN samples exhibited monoclinic symmetry (JCPDS PDF#77-1098). For KNN-6, the broad diffraction peak at 45° indicated more than one diffraction peak overlapped there. The split diffraction peaks at 23° and 45° indicated that the space group of the as-synthesized sample was orthorhombic or monoclinic symmetry rather than cubic symmetry.[40] As it is known the crystal symmetry of the orthorhombic and monoclinic space groups was much lower than that of the cubic space group. Therefore, the KNN samples exhibited a stronger piezoelectric effect due to their non-centrosymmetric structures, which played an important role in the piezo-enhanced photocatalytic process. To obtain the optimal hydrothermal reaction temperature, we also synthesized KNN samples at different hydrothermal temperatures and the XRD patterns are shown in Fig. S1.† As shown in Fig. S1,† when the hydrothermal temperatures were below 200 °C, the final product was $(K,Na)Nb_6O_{19}$ (JCPDS: No.14-0360) rather than $(K,Na)NbO_3$ due to the lack of activation energy for the whole reaction.

We used XPS to investigate the element information at the surface of KNN-6 ($K_{0.4}Na_{0.6}NbO_3$), which is shown in Fig. 2. The XPS survey scan spectrum of the KNN-6 samples exhibited distinct Na, K, Nb, and O core level peaks, without any additional peaks remaining, which was consistent with the results of EDS listed in Table 2. Fig. 2(b) shows the binding energies of Nb $3d_{5/2}$ and Nb $3d_{3/2}$ at 206.1 and 208.7 eV respectively, which were the characteristic peaks for the Nb^{5+} ion.[29] As shown in Fig. 2(c), there were 4 binding energy peaks for the K 2p energy levels, indexed as K $2p_{3/2}$, K $2p_{1/2}$, K $2p'_{3/2}$,

and K $2p'_{1/2}$ at 290.9 eV, 293.6 eV, 292.6 and 295.3 eV, respectively. The K 2p' binding energies that were not detected in pure $KNbO_3$[28] samples might be caused by the interaction between the K and Na elements, which was consistent with a previous report on the KNN sample.[30] The binding energy for Na 1s at 1070.5 eV was not deconvoluted, which was consistent with the results presented in other reports.[28,29]

The morphologies of the as-synthesized KNN samples were first investigated *via* SEM. Fig. 3(a)–(g) show the SEM images of the as-synthesized KNN samples. As shown in Fig. 3(a) and (b), for KNN-0 and KNN-5, due to a large amount of Na element, the KNN particles were in cubic shapes with an average size of ~2 μm, which was similar to that of $NaNO_3$. When the ratio of KOH/NaOH in the reactant reached 6/4, due to the increased contents of K element, the morphologies of the as-synthesized KNN-6 samples ($K_{0.4}Na_{0.6}NbO_3$) were in regular octahedron shapes with an average size of ~4 μm. As shown in Fig. 3(c), each single KNN-6 octahedron was assembled by cubic KNN-6 nanoparticles with sizes of about 50 nm, which is highlighted with a red circle, and this made the surface coarse. As the edges and corners could act as the active sites for MB absorption and degradation, the KNN-6 samples with abundant edges and corners exhibited a better degradation efficiency than other KNN samples. For KNN-7 (Fig. 3(d)) and KNN-8 (Fig. 3(e)), the morphologies were octahedra with missed vertexes, which might be related to the changes of surface-active energies when increasing the K content in KNN. For KNN-9 (Fig. 3(f)) and KNN-10 (Fig. 3(g), pure $KNbO_3$), the shapes were backed to cubic with an average size of ~1 μm, which were similar to the morphologies of $KNbO_3$ owing to its high K element content. The EDS results presented in Table 2 showed the actual atomic ratios of Na/K in different KNN samples. When the atomic ratio of KOH/NaOH in the reactant was lower than 1/1 (KNN-0 and KNN-5),
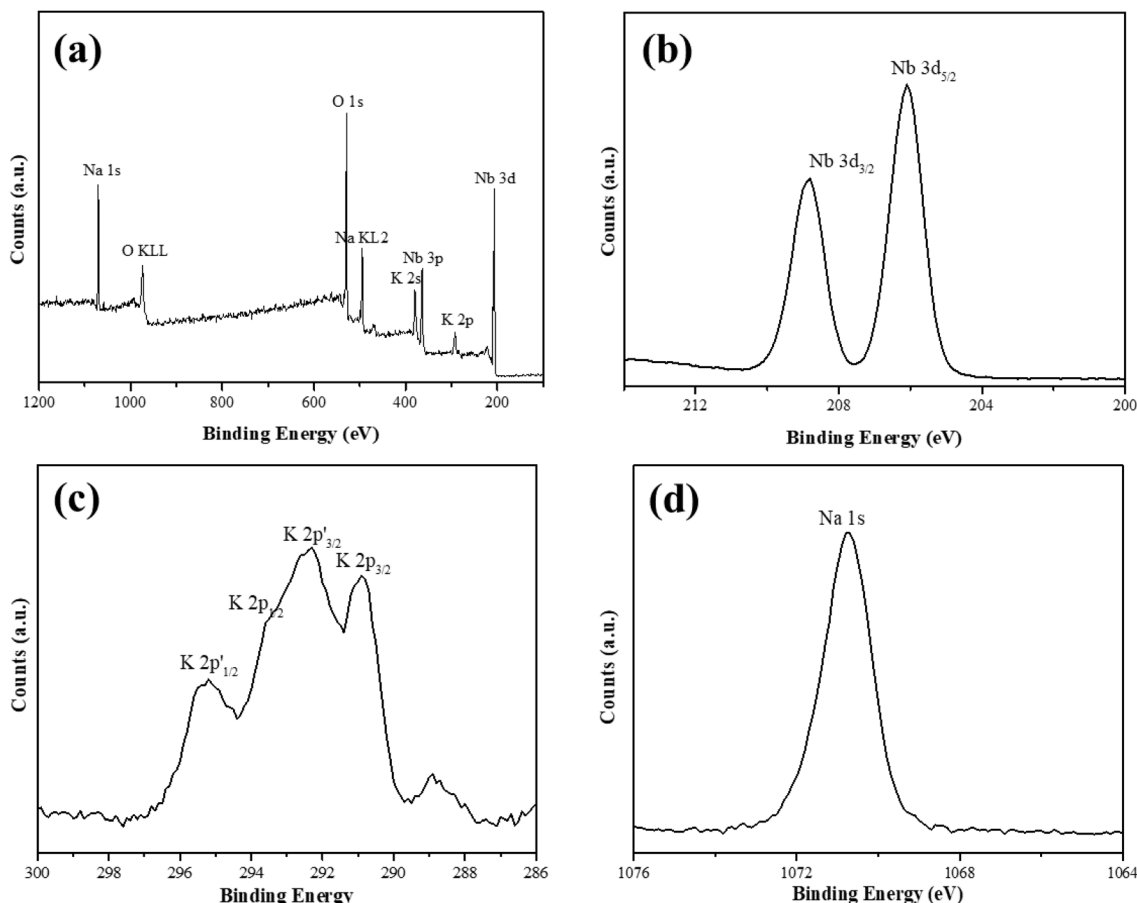
Fig. 2 (a) XPS patterns of the as-synthesized KNN-6 microstructures showing the presence of O, Nb, K and Na elements; (b) Nb 3d at 206.1 and 208.7 eV; (c) K 2p at 290.9 eV and 293.6 eV; K 2p' at 292.6 and 295.3 eV; and (d) Na 1s at 1070.5 eV.

Table 2 EDS results of different KNN samples

	Na (atom%)	K (atom%)	Nb (atom%)	O (atom%)	K/(K + Na)	(K + Na)/Nb
KNN-0	16.30	0	19.76	63.94	0	0.8249
KNN-5	13.76	1.17	18.00	67.07	0.0784	0.8294
KNN-6	10.73	6.94	19.02	63.31	0.3928	0.9290
KNN-7	5.03	11.40	18.21	65.36	0.6939	0.9023
KNN-8	3.66	14.41	20.15	61.79	0.7975	0.8968
KNN-9	1.87	15.92	19.26	62.95	0.8949	0.9237
KNN-10	0	17.00	17.30	65.70	1	0.9827

the contents of the K element in the final KNN products were tiny. However, upon further increasing the KOH content in the reactant, the content of the K element in the final products could be increased evidently. The main reason was that the reactivity of Na^+ per mole was much stronger than that of K^+, and when they coexisted in solution, the Na^+ would react with Nb_2O_5 first due to its stronger reactivity. As the reaction proceeded, the concentration of Na^+ decreased continuously, which led to a decrease in Na^+ reactivity. When the concentration of Na^+ decreased to a certain extent, the reaction activity of Na^+ became lower than that of K^+. Thus K^+ could not

react with Nb_2O_5 until the reactivity of Na^+ was lower than that of K^+. Therefore, only a few K elements were found in KNN-0 and KNN-5 due to the insufficient amount of K^+.

The morphologies of KNN-6 powders were further investigated by TEM, HRTEM and SAED. As shown in Fig. 3(h), the cubic-shaped projection of the KNN-6 octahedron along two opposite vertices could be clearly seen *via* the contrast between the black center and the light edges. The rough edges were consistent with the SEM images in Fig. 3(c). As the KNN-6 micro-octahedra were assembled by ~50 nm cubic KNN-6 nanoparticles, Fig. 3(i) and (j) show the SAED and
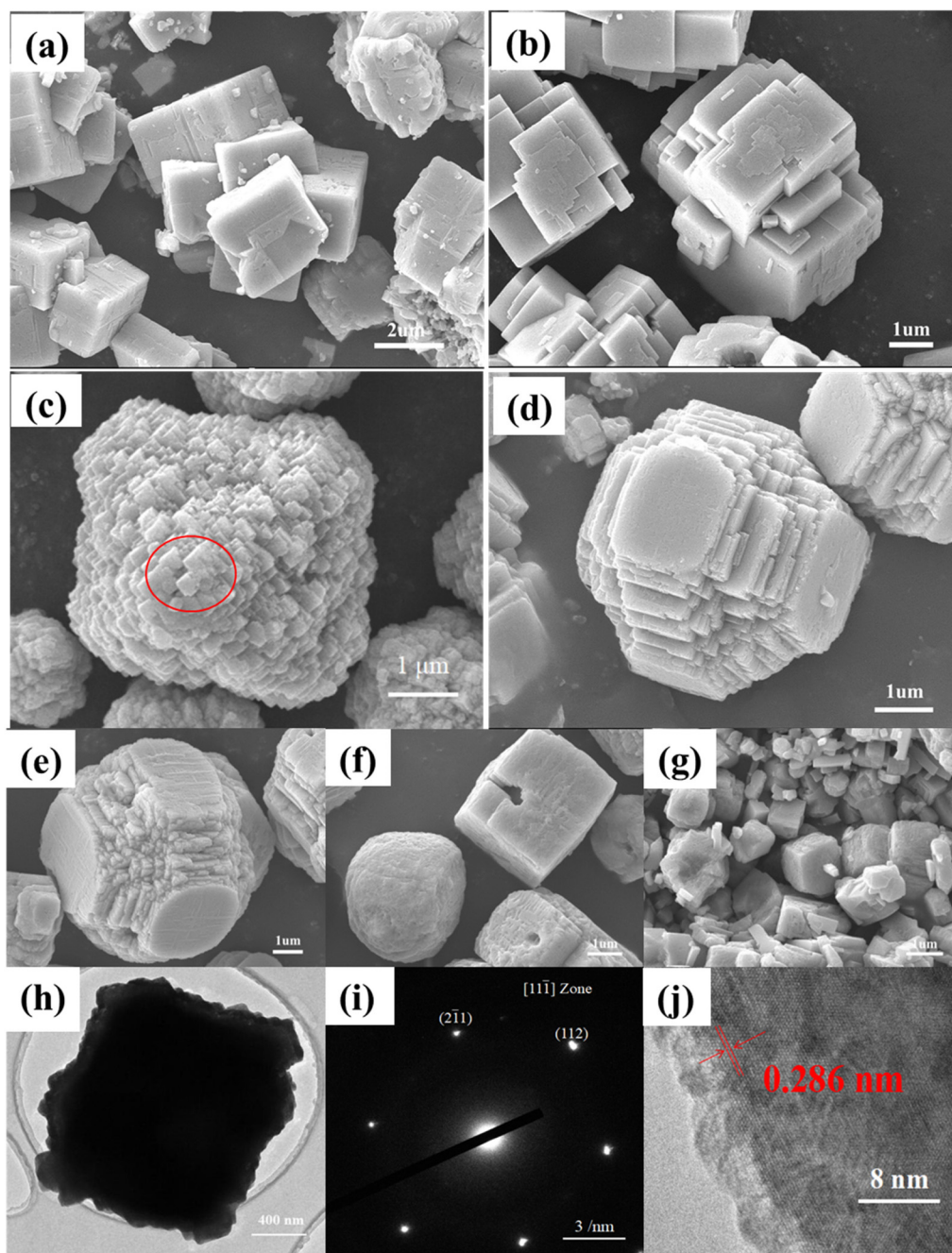
Fig. 3 The morphology of the as-synthesized KNN samples. (a)–(g) SEM images of KNN powders with different Na/K ratios: (a) KNN-0, (b) KNN-5, (c) KNN-6, (d) KNN-7, (e) KNN-8, (f) KNN-9, and (g) KNN-10; (h) TEM image of the KNN-6 samples, the cubic shaped projection of the KNN-6 octahedron could be clearly seen; (i) SAED pattern of KNN-6, the zone axis was indexed as $\langle 11\bar{1} \rangle$ with (112) and ($2\bar{1}1$) spots around the center incident spot; (j) HRTEM image of a KNN-6 nanoparticle on the edge, the lattice spacing of 0.286 nm indicated the (020) lattice plane.

HRTEM images of individual cubic KNN-6 nanoparticles. As shown in Fig. 3(i), two spots around the (000) spot were indexed as (112) and ($\bar{2}1\bar{1}$), indicating that the zone axis of the SAED pattern was $\langle 11\bar{1} \rangle$. As measured from the HRTEM image in Fig. 3(j), one lattice spacing of the individual cubic KNN-6 nanoparticles was 0.286 nm, which was indexed to the (020) lattice plane of orthorhombic KNN. This indicated that the exposed facet of the KNN cubic nanoparticles was (020). As the (020) crystal plane was perpendicular to the spontaneous

polarization (P) direction of $KNbO_3$,[28] the KNN-6 octahedron assembled by cubic KNN-6 nanoparticles with (020) exposed facets had better piezoelectric properties, which was also consistent with the PFM results presented in Fig. 5.

Formation mechanism of KNN octahedra

A series of time-dependent hydrothermal reactions were carried out to investigate the formation mechanism of KNN-6

octahedra. Their phase structures and morphologies are separately shown in Fig. S2 and S3.† After one hour of reaction, only the cobblestone-like particles can be observed in Fig. S3(a),† which was indexed as the intermediate product of $(K,Na)Nb_6O_{19}$ according to the XRD pattern in Fig. S2.† As highlighted with red circles in Fig. S3(b),† after two hours of reaction, a few irregular-shaped KNN-6 microparticles assembled by small nanocubes were observed. As the hydrothermal reaction prolonged to 4 hours, an increasing number of KNN-6 microparticles stacked by small nanocubes were formed. Meanwhile, as shown in Fig. S2,† a small diffraction peak at 23° appeared (highlighted with a red circle), which was assigned to the diffraction peaks of KNN, indicating that the cobblestone-like intermediate products $(K,Na)Nb_6O_{19}$ began to evolve into octahedron-like KNN after 4 hours of reaction. When the hydrothermal time was over 8 hours, almost all the cobblestone-like intermediate products $(K,Na)Nb_6O_{19}$ had been transformed into octahedron-like KNN, which was consistent with the XRD patterns in Fig. S2.†

Based on the evolution of KNN morphologies under different reaction times (1 h–24 h) presented in Fig. S3,† we proposed a dissolution and recrystallization mechanism to illustrate the formation process of KNN-6 octahedra.[41] At the first stage of the hydrothermal reaction, $Nb_6O_{19}{}^{8-}$ was first formed *via* the reaction between Nb_2O_5 and OH^-, and then the cobblestone-like intermediate products $(K,Na)Nb_6O_{19}$ were precipitated, as shown in Fig. S3(a)–(c).† However, the intermediate products $(K,Na)Nb_6O_{19}$ could transform into stable structures $(K,Na)NbO_3$ by overcoming the energy barrier. When the hydrothermal time was less than 4 h or the temperature was below 200 °C, the whole reaction energy was insufficient to transform $(K,Na)Nb_6O_{19}$ into $(K,Na)NbO_3$, which corresponded to the results shown in Fig. S1–S3.† When the hydrothermal time was longer than 4 h, the cobblestone-like $(K,Na)Nb_6O_{19}$ began to be dissolved in the alkali solution again to precipitate out a more stable phase of $(K,Na)NbO_3$ nuclei with an average size of 50 nm. As the exposure facet of KNN nanosized nuclei had a higher energy, these KNN nuclei would aggregate together to form an octahedron-like unit spontaneously to reduce the surface energy as the reaction proceeded. The whole formation process is illustrated in Fig. S3(g).†

Optical and piezoelectrical properties of KNN

The light absorption properties and the band gap structures of all the KNN samples were characterized *via* UV-vis diffuse reflectance spectroscopy (DRS) and are presented in Fig. 4. Fig. 4(a) shows the UV-vis light absorption curves of all the KNN samples. From the figure, we could find that $NaNbO_3$ (KNN-0) had the weakest absorption edge at 380 nm, indicating that $NaNbO_3$ had the widest band gap. For KNN-6 and KNN-7, the intensities of light absorption peaks were relatively higher than that of other KNN samples, indicating their high light absorption efficiency, which was conducive to their photocatalytic performances.

The optical bandgap of the KNN was determined using the Kubelka–Munk function,

$$\alpha h v = A(h v - E_g)^{1/2} \qquad (2)$$

where α represents the absorption coefficient; h stands for Plank's constant; A is the absorbance; v stands for the light frequency; and E_g is the band gap value.

We calculated the band gaps of all KNN samples *via* the Kubelka–Munk transformed reflectance spectra. As shown in Fig. 4(b), the $(\alpha h v)^2$ values changed with the $h v$ values linearly, thus the intercept of the fitted straight slope line with the x-axis was the band gap value. From our calculations, the band gap values of KNN samples ranged from 3.12 eV to 3.47 eV depending on the K element content in KNN samples. Among them, the pure $NaNbO_3$ (KNN-10) had the widest band gap of 3.47 eV. While for KNN-6, the band gap was as narrow as 3.2 eV. KNN-6 with a smaller band gap could absorb a broader portion of sunlight and thus is more favorable for the efficient utilization of solar energy. Therefore, the high light absorption
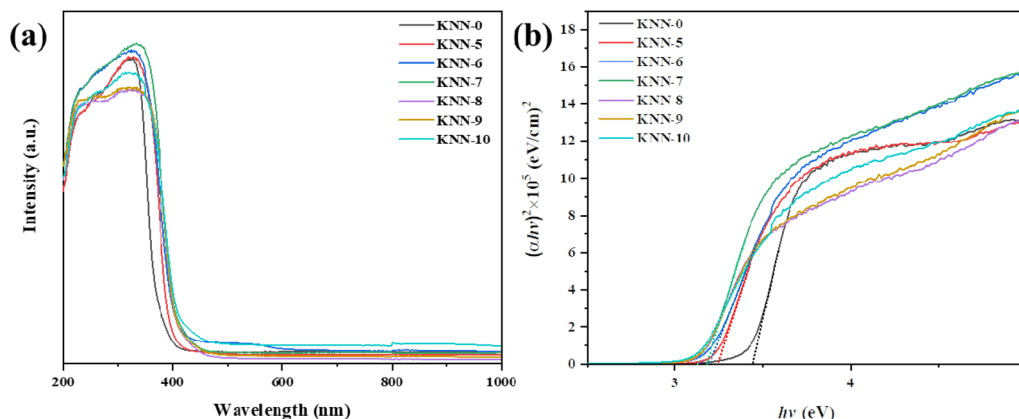

Fig. 4 (a) The UV-vis absorption curves of KNN samples with different Na/K ratios. (b) The corresponding Kubelka−Munk (K−M) transformation curves of different KNN powders. The calculated band gaps for the KNN samples ranged from 3.1 to 3.4 eV.
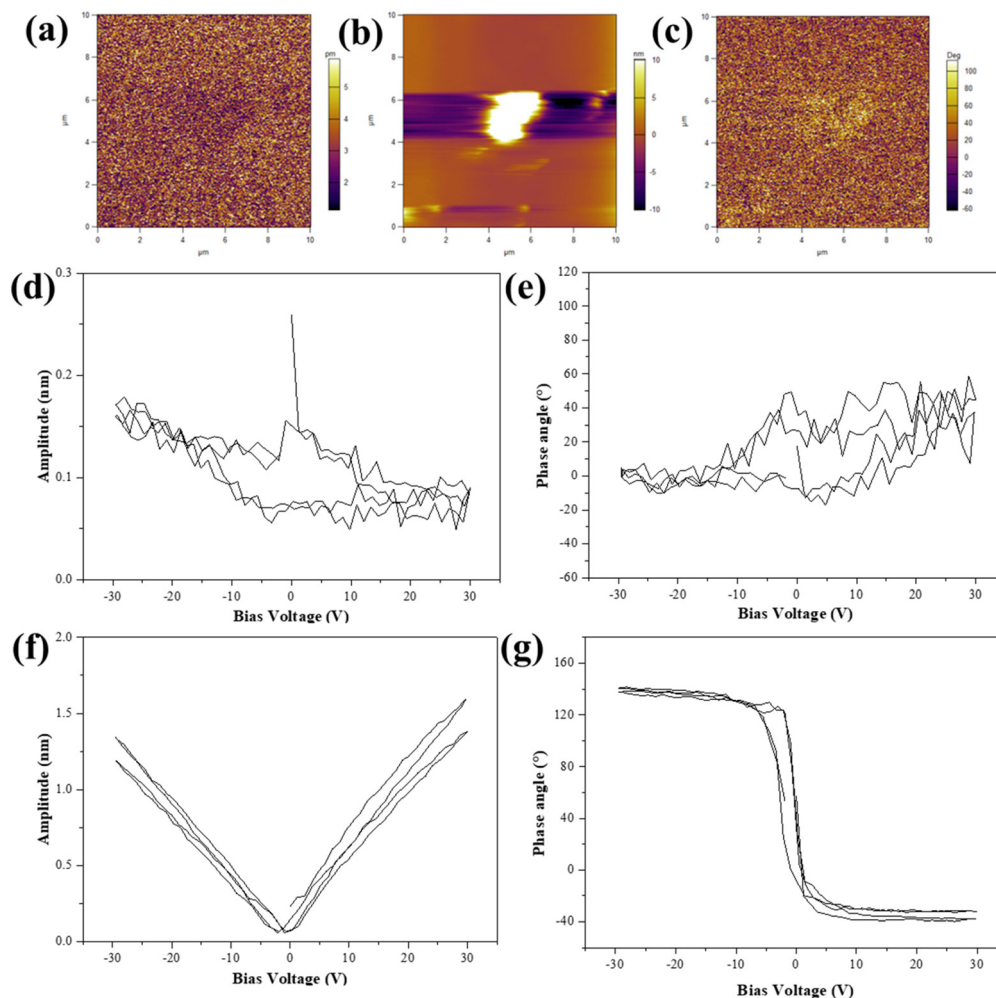
Fig. 5 PFM characterization results of the KNN-6 microstructures. (a) amplitude, (b) topographic, and (c) phase images of the KNN-6 sample; (d) the piezoelectric amplitude and (e) phase transformation under a bias voltage of 30 V in the "OFF" state; (f) the piezoelectric amplitude and (g) phase transformation under a bias voltage of 30 V in the "ON" state.

rate and narrow band gap caused the improved photocatalytic performance of KNN-6.

As a kind of ferroelectric material, we used the PFM to investigate the ferroelectric properties of the KNN samples. In this report, KNN-6 was selected to investigate its piezoelectric properties. The topographic and phase images and the amplitude of KNN-6 samples are shown in Fig. 5(a)–(c) respectively. The contour of a single KNN sample with a cubic shape could be clearly observed in the topographic image. The piezo response of the KNN sample was also detected by applying a bias voltage of 30 V. The obtained PFM amplitude and phase signals of the KNN sample are shown in Fig. 5(d)–(g) in the "OFF" state (only piezoelectric displacement) and the "ON" state (the DC offset voltage was applied to largely amplify the piezoelectric displacement), respectively. Due to its large size and rough surface, the measurement error was large (Fig. 5(d) and (e)). The PFM amplitude and phase signals of the KNN-6 sample in the "OFF" state were not obvious. Therefore, the DC offset

voltage was used to amplify the piezoelectric displacement which showed a perfect piezoelectric displacement in Fig. 5(f) and (g) (the "ON" state). Fig. 5(d) and (e) also presented a localized hysteresis loop about 80° reverse when the DC bias voltage was established between −30 V and +30 V, which suggested the occurrence of a local polarization switching process and the ferroelectric nature of KNN samples.[42,43]

Piezo-/photocatalytic performance for MB degradation

The degradation of MB under light irradiation without adding any catalyst is shown in Fig. S4,† from which we can see that nearly no MB (less than 10%) was degraded only under light irradiation. The photocatalytic and piezo-photocatalytic properties of the as-synthesized samples (KNN-0 to KNN-10) under different catalytic conditions (solely irradiation or vibration, irradiation together with vibration) were determined via the degradation of MB (methylene blue)
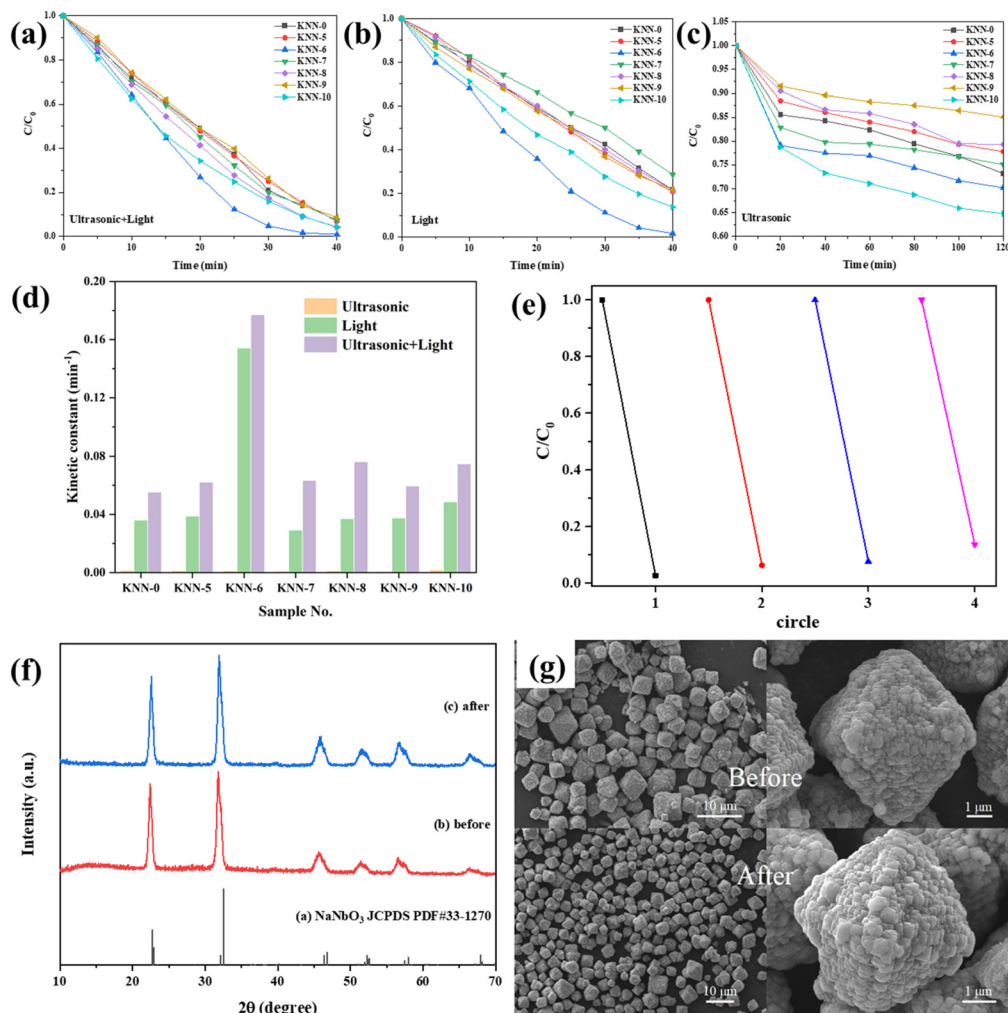
Fig. 6 The degradation efficiencies of KNN crystals with different Na/K ratios under (a) both light irradiation & ultrasonic vibration, (b) solely light irradiation, and (c) solely ultrasonic vibration. For KNN-6, it showed the best degradation efficiency and about 99.7% of MB were degraded within 40 minutes under the synergistic effect of light irradiation and ultrasonic vibration. (d) The kinetic constants *k* of KNN crystals with different Na/K ratios. Under both light irradiation & ultrasonic vibration, the kinetic constants were enhanced remarkably compared to those under only light irradiation. (e) The recyclability tests of the KNN-6 microstructures. After four cycles of catalysis, the KNN-6 sample remained stable. There were no obvious changes in the phase (f) and morphology (g) of the KNN-6 microstructures before and after 4 cycles of degradation.

solutions and are summarized in Fig. 6. The detailed UV-vis absorption spectra for MB solution degraded by different KNN samples under the synergistic effect of light irradiation and ultrasonic vibration are shown in Fig. S5.† The characteristic UV-vis absorption peaks for MB at ~660 nm were continuously decreased as the reaction proceeded. According to eqn (1), their MB degradation efficiencies were calculated and are presented in Fig. 6(a). From Fig. 6(a) we can find that, under the combined effects of light irradiation and ultrasonic vibration, all the KNN samples (KNN-0 to KNN-10) could degrade more than 90% of MB within 40 min. Among them, the KNN-6 samples exhibited the best degradation efficiency, which could degrade ~90% of MB within 25 minutes and ~99.7% at the time of 40 minutes, and then the MB solution could be deemed as completely cleaned. As a comparison, the degradation efficiencies of MB by KNN

samples under solely UV-light irradiation or ultrasonic vibration are also summarized in Fig. 6(b) and (c), and their detailed UV-vis absorption spectra are presented in Fig. S6 and S7,† respectively. Fig. 6(b) shows that, under sunlight irradiation, the KNN-6 sample still exhibited an excellent degradation efficiency and could clean ~97% of MB solution within 40 min. However, the MB degradation efficiencies of other KNN samples decreased after removing the ultrasonic vibrations. For example, the KNN-7 sample could degrade about 90% of MB within 40 minutes under both light irradiation and ultrasonic vibration, but only ~70% under light irradiation alone. This demonstrated that the piezoelectric effect could obviously enhance the photocatalytic degradation efficiencies of KNN samples. As shown in Fig. 6(c) and Fig. S7,† only negligible MB was degraded under ultrasonic vibration without light irradiation, which demonstrated

that photocatalysis rather than piezo catalysis played the key role in the MB degradation process of KNN.

Since the concentration of MB solution was very low (10 mg L^{-1}), the degradation process could be recognized as a kind of pseudo-first-order reaction. Therefore, the value of $\ln(C_0/C)$ should be linearly correlated with the degradation time. The ratio of $\ln(C_0/C)$ to degradation time (t) was defined as the kinetic constant k, and a higher k indicates a higher degradation efficiency. The kinetic constant values for all the KNN samples were calculated from Fig. 6(a)–(c) and are summarized in Table 3 and Fig. 6(d). As shown in Fig. 6(d), the kinetic constants of KNN under only ultrasonic vibration were quite low. Under the combined effect of irradiation and vibration, the kinetic constants increased largely by 50%–100% compared to those only under light irradiation, which was consistent with the results in Fig. 6(a)–(c). In Fig. 6(e), the repeatability and recycling stability of KNN-6 for wastewater treatment were examined. The detailed UV-vis absorption curves are presented in Fig. S8.† The results showed that the degradation efficiency of KNN-6 was very stable and no obvious deterioration in catalytic performance was observed after 4 cycles of degradation. In addition, we also examined the phase structures and morphologies of the KNN-6 specimens by XRD and SEM after degradation. As shown in Fig. 6(f) and (g), there were nearly no changes in the phase (XRD pattern, (f)) and morphology (SEM image, (f)) of KNN-6 microstructures before and after degradation, demonstrating the excellent stability of KNN-6 catalysts.

Roles of oxidative radicals in photocatalysis

Given the crucial role of oxidative radicals in photocatalysis,[23] we detected the contents of $^\bullet OH^-$ and $^\bullet O_2^-$ radicals under two degradation conditions (light irradiation, light irradiation & ultrasonic vibration) and made a comparison. Although the exact concentration of $^\bullet OH^-$ and $^\bullet O_2^-$ radicals cannot be directly obtained, we can estimate their relative concentration *via* the reaction between the radicals and reagents such as NBT or TA. For the detection of hydroxyl radicals ($^\bullet OH^-$), we used TA as the trapping agent to determine its concentration. Typically, we dissolved TA in NaOH to form a TA-NaOH solution and then dispersed the KNN-6 sample in it. The $^\bullet OH^-$ radicals generated under irradiation or vibration & irradiation could react with TA to form an oxidized product of TAOH, which shows a strong PL fluorescent peak at 425 nm. The stronger the PL peak intensities at 425 nm, the higher the concentration of $^\bullet OH^-$ radicals. Therefore, the concentrations of the generated $^\bullet OH^-$ radicals in water could be reflected by the PL peak intensities at 425 nm. As shown in Fig. 7(a) and

(b), the intensities of PL fluorescence responses at 425 nm became stronger with the prolonging of the degradation time, indicating the formation of the $^\bullet OH^-$ radicals during the degradation process. Moreover, the PL peak intensities of TAOH under irradiation & vibration (10 800 counts) were much stronger than that under only light irradiation (6200 counts), which indicated that more $^\bullet OH^-$ radicals were generated with the assistance of ultrasonic vibration. As NBT was a kind of O_2^- sensitive dye, it can be rapidly degraded in the presence of O_2^- radicals. Therefore, the relative concentration of $^\bullet O_2^-$ radicals could be estimated using the degradation rate of NBT. As shown in Fig. 7(c) and (d), ~82% of NBT was degraded within 10 minutes under both irradiation and vibration. In contrast, only ~76% of NBT was degraded after 60 minutes under light irradiation only, which indicated that more O_2^- radicals were generated under both irradiation and vibration. The results shown in Fig. 7(a–d) demonstrate that under the synergistic effect of ultrasonic vibration and irradiation, more oxidative radicals such as $^\bullet O_2^-$ and $^\bullet OH^-$ were generated.

To figure out which kind of radicals among $^\bullet O_2^-$, $^\bullet OH^-$ and h^+ played the most important role in the degradation process, we further performed free radical trapping experiments by adding different scavengers into MB solutions and examining their degradation efficiencies. According to previous research, radical scavengers BQ, TBA and EDTA-2Na can effectively trap $^\bullet O_2^-$, $^\bullet OH^-$ and h^+, respectively.[23] As shown in Fig. 7(e) (the detailed absorption curves are shown in Fig. S9†), by adding them separately into the MB solutions, the degradation efficiencies were compromised to different extents, which denoted that all these three oxidative radicals could promote the degradation process. Among them, the MB degradation efficiency was the lowest when scavenger BQ was added, which indicated that compared with other radicals, $^\bullet O_2^-$ played the most crucial role in the degradation process.

Piezo enhanced photocatalysis of KNN

In this work, we used ultrasonic vibration to simulate the external stress field to promote the photocatalysis process. When the MB solutions containing KNN samples were placed in an ultrasonic environment, bubbles were formed, grew and ruptured at the KNN surfaces. Upon the rupture of the bubbles, a localized high pressure together with a high-velocity jet of liquid was generated at the KNN surfaces.[28] As a kind of piezoelectric and ferroelectric material, the KNN crystals could be easily polarized and orderly arranged along the piezoelectric field direction, which could lead to the accumulation of piezo-generated charges on the crystal surfaces. In this work,

Table 3 The kinetic constant (k) values of the KNN samples with different Na/K ratios

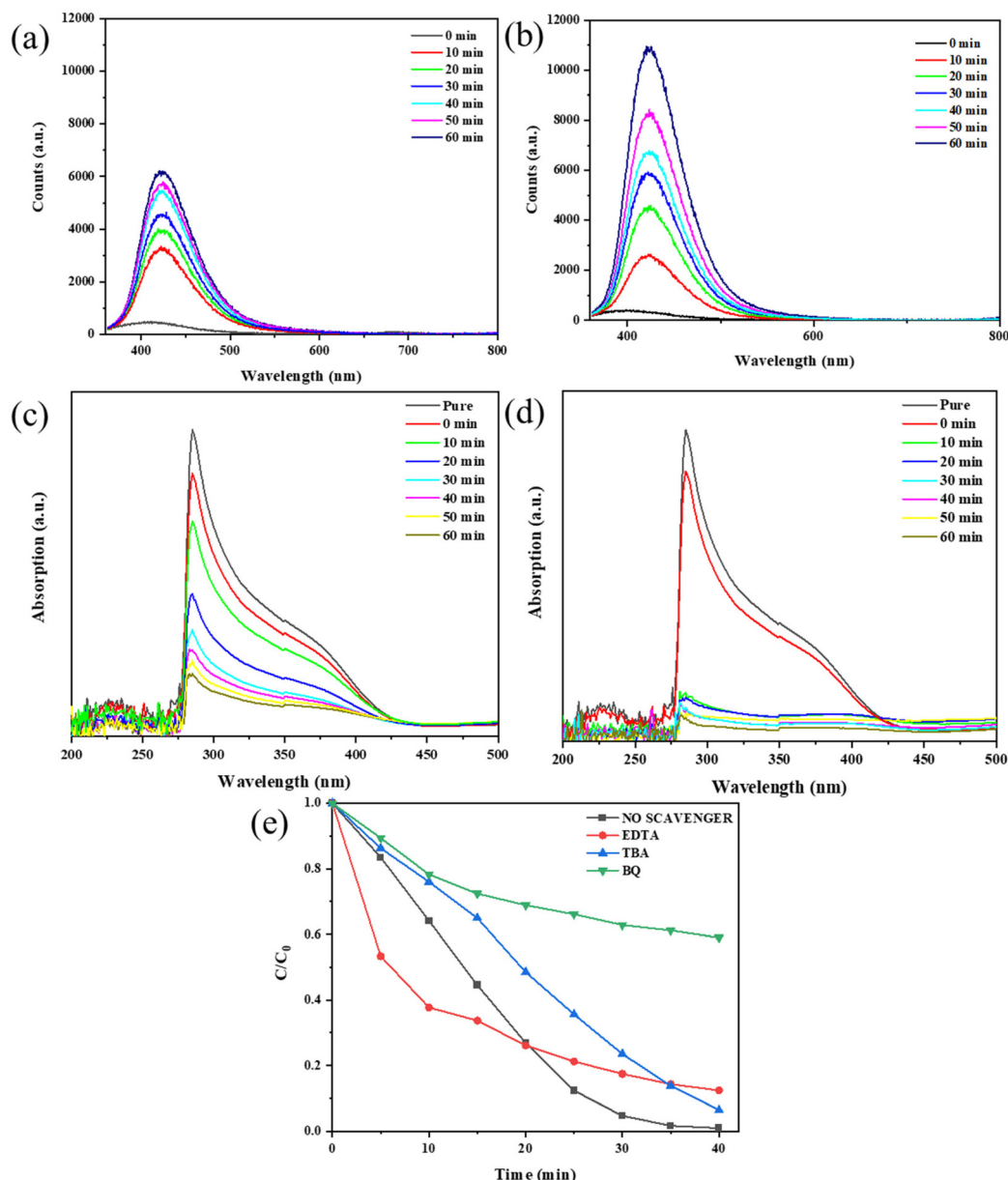| Sample no.	KNN-0	KNN-5	KNN-6	KNN-7	KNN-8	KNN-9	KNN-10
Ultrasonic (min^{-1})	0.00156	0.0013	0.00131	0.000893	0.00135	0.000695	0.0019
Light (min^{-1})	0.03606	0.03881	0.15419	0.02913	0.03703	0.03758	0.04858
Ultrasonic + Light (min^{-1})	0.05524	0.06207	0.17709	0.06334	0.07617	0.05943	0.07479

Fig. 7 The PL spectra of TAOH under (a) light irradiation and (b) light irradiation & ultrasonic vibration. The NBT degradation efficiencies of KNN-6 under (c) light irradiation and (d) light irradiation & ultrasonic vibration. (e) The degradation efficiencies of MB of KNN-6 in the presence of different scavengers. A sharp decline in the degradation efficiency of KNN-6 in the presence of BQ means that the $\cdot O_2^-$ played the most important role in the piezo-photodegradation process.

the photocatalytic degradation efficiency could be largely enhanced by the piezoelectric effect; therefore, we proposed a possible mechanism to illustrate this synergistic effect in Fig. 8, which depicts the following three aspects. First, the induced piezoelectric field could increase the concentration of the photo-generated electrons and holes, which played an important role in MB degradation. For conventional photocatalysts, the photogenerated electron–hole pairs tended to recombine owing to their opposite electric charges. However, as a piezo-photocatalytic material, under ultrasonic vibration, the positive and negative charges can be generated at the surface

of KNN samples. On one hand, due to the electrostatic force, the photogenerated electrons will be attracted by piezo-generated positive charges and repelled by piezo-generated negative charges; on the other hand, the photogenerated holes will be attracted by piezo-generated negative charges and repelled by piezo-generated positive charges. Therefore, the electric field induced by the piezoelectric effect can prevent the recombination of photogenerated electrons and holes. Second, as reported in a previous work, the energy band structure would be affected under external stress.[44] Specifically, the positions of the valence band (VB) and the conduction band (CB) would
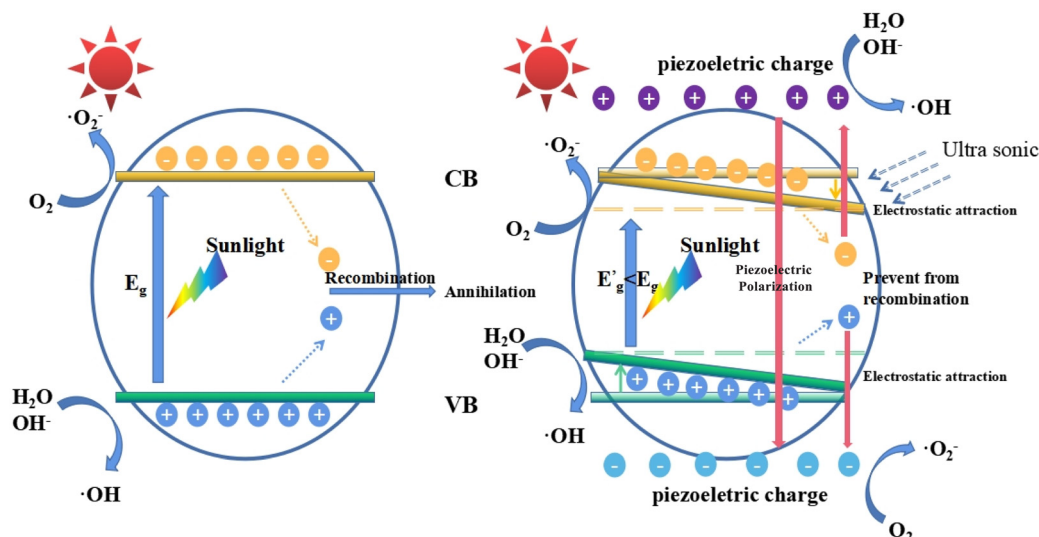
Fig. 8 The piezoelectrically enhanced photo-catalysis mechanism of KNN-6.

be tilted by the internal piezoelectric field. As a result, the gap between the highest position of the VB and the lowest position of the CB will be closer than that without the introduction of external stress, indicating a decreased equivalent band gap under ultrasonic vibration, which made electrons much easier to be excited from the VB to the CB. Third, owing to the screening effect, the high energy piezoelectric electrons can be generated at the surface of KNN samples and react with H_2O and O_2 to form oxidative radicals such as $\cdot O_2^-$ and $\cdot OH^-$, which can oxidize the dye molecules in solutions effectively.[29,43,45]

In this work, among all the KNN samples, the KNN-6 samples ($K_{0.4}Na_{0.6}NbO_3$) had the best piezo-photocatalytic property. As shown in Fig. 3, the KNN-6 microstructures were stacked by cubic KNN-6 nanoparticles with sizes of ~50 nm. The low magnification SEM images (Fig. S10†) demonstrate that all the KNN-6 particles are of homogeneous and uniform octahedral shape. Therefore, large amounts of edges and corners were formed on the microstructure surfaces and acted as the active sites for absorption and catalysis degradation.[46] In addition, the (010) exposed facet for the KNN-6 nanocubes was alongside one of the polarization components of $KNbO_3$, which was conducive to its piezoelectric effect.[28] Lastly, compared to other micrometer scale KNN samples, the constituent particles of the KNN-6 octahedra were at nanometer scales, which could make the photogenerated electrons and holes migrate to the surface easily. The size effect caused the easy separation of holes and electrons could also benefit the catalytic reactions effectively.

Conclusions

In this report, using the environmentally friendly hydrothermal strategy, we synthesized a kind of KNN microstructure as piezoelectrically enhanced effective photocatalysts for wastewater treatment. By changing the ratios of KOH/NaOH in the reactant, a series of KNN samples with different K/Na ratios marked as KNN-0 to KNN-10 were obtained. Among them, the octahedron-shaped KNN-6 sample ($K_{0.4}Na_{0.6}NbO_3$) exhibited the best piezo- photocatalytic performance due to its high light utilization rate, narrow band gap structure, and excellent piezoelectric properties. Under the combined effects of light irradiation and ultrasonic vibration, about 99% of MB could be degraded by KNN-6 microstructures within 40 minutes, which was several times faster than that reported in previous works. In addition, the as-prepared KNN-6 microstructures could retain their outstanding piezo-photocatalytic capability after several rounds of cyclic tests, which demonstrated their excellent stability when used for wastewater purification. This work offered a new piezo-photocatalyst with excellent catalytic degradation efficiency of organic dyes, which holds great potential in the field of environmental protection. In addition, the proposed "dissolution and recrystallization" formation mechanism of KNN octahedra also provided a new way for morphology control in materials synthesis engineering.

Conflicts of interest

There are no conflicts to declare.

Acknowledgements

References

1 Y. Lai, L. Sun, Y. Chen, H. Zhuang, C. Lin and J. Chin, Effects of the Structure of TiO_2 Nanotube Array on Ti Substrate on Its Photocatalytic Activity, *J. Electrochem. Soc.*, 2006, **153**, D123–D127.

2 J. Cai, J. Huang and Y. Lai, 3D Au-decorated $BiMoO_6$ Nanosheet/TiO_2 Nanotube Array Heterostructure with Enhanced UV and Visible-light Photocatalytic Activity, *J. Mater. Chem. A*, 2017, **5**, 16412–16421.

3 J. Guan, Y. Jia, T. Chang, L. Ruan, T. Xu, Z. Zhang, G. Yuan, Z. Wu and G. Zhu, Highly Efficient Piezo-catalysis of the Heat-treated Cellulose Nanocrystal for Dye Decomposition Driven by Ultrasonic Vibration, *Sep. Purif. Technol.*, 2022, **286**, 120450.

4 Y. Zhang, Q. Wang, J. Lu, Q. Wang and Y. Cong, Synergistic Photoelectrochemical Reduction of Cr(VI) and Oxidation of Organic Pollutants by g-C_3N_4/TiO_2-NTs Electrodes, *Chemosphere*, 2016, **162**, 55–63.

5 R. Guo, R. Tian, D. Shi, H. Li and H. Liu, S-Doped, $ZnSnO_3$ Nanoparticles with Narrow Band Gaps for Photocatalytic Wastewater Treatment, *ACS Appl. Nano Mater.*, 2019, **2**, 7755–7765.

6 Y. Hu, Y. Chang, P. Fei, R. Snyder and Z. Wang, Designing the Electric Transport Characteristics of ZnO Micro/Nanowire Devices by Coupling Piezoelectric and Photoexcitation Effects, *ACS Nano*, 2010, **4**, 1234–1240.

7 L. Pan, S. Sun, Y. Chen, P. Wang, J. Wang, X. Zhang, J.-J. Zou and Z. L. Wang, Advances in Piezo-Phototronic Effect Enhanced Photocatalysis and Photoelectrocatalysis, *Adv. Energy Mater.*, 2020, **10**, 2000214.

8 A. Kubacka, M. Fernández-García and G. Colón, Advanced Nanoarchitectures for Solar Photocatalytic Applications, *Chem. Rev.*, 2012, **112**, 1555–1614.

9 Y. Zhao, Z.-B. Fang, W. Feng, K. Wang, X. Huang and P. Liu, Hydrogen Production from Pure Water via Piezoelectric-assisted Visible-light Photocatalysis of CdS Nanorod Arrays, *ChemCatChem*, 2018, **10**, 3397–3401.

10 Y.-C. Wang and J. M. Wu, Effect of Controlled Oxygen Vacancy on H2-Production through the Piezocatalysis and Piezophototronics of Ferroelectric R3C $ZnSnO_3$ Nanowires, *Adv. Funct. Mater.*, 2020, **30**, 1907619.

11 M. Ismail, Z. Wu, L. Zhang, J. Ma, Y. Jia, Y. Hu and Y. Wang, High-Efficient Synergy of Piezocatalysis and Photocatalysis in Bismuth Oxychloride Nanomaterial for Dye Decomposition, *Chemosphere*, 2019, **228**, 212–218.

12 J. Zhao, L. Chen, W. Luo, H. Li, Z. Wu, Z. Xu, Y. Zhang, H. Zhang, G. Yuan, J. Gao and Y. Jia, Strong Tribo-catalysis of Zinc Oxide Nanorods via Triboelectrically-harvesting Friction Energy, *Ceram. Int.*, 2020, **46**, 25293–25298.

13 L. Ruan, Y. Jia, J. Guan, B. Xue, S. Huang, Z. Wang, Y. Fu and Z. Wu, Tribo-Electro-Catalytic Dye Degradation Driven by Mechanical Friction using MOF-Derived $NiCo_2O_4$ Double-Shelled Nanocages, *J. Cleaner Prod.*, 2022, **345**, 131060.

14 Y. Yao, Y. Jia, Q. Zhang, S. Li, G. Li, X. Cui and Z. Wu, Piezoelectric $BaTiO_3$ with the Milling Treatment for Highly Efficient Piezocatalysis under Vibration, *J. Alloys Compd.*, 2022, **905**, 164234.

15 Q. Zhang, Y. Jia, X. Wang, L. Zhang, G. Yuan and Z. Wu, Efficient Tribocatalysis of Magnetically Recyclable Cobalt Ferrite Nanoparticles through Harvesting Friction Energy, *Sep. Purif. Technol.*, 2023, **307**, 122846.

16 L. Ruan, Y. Jia, J. Guan, B. Xue, S. Huang, Z. Wu, G. Li and X. Cui, Highly Piezocatalysis of Metal-Organic Frameworks Material ZIF-8 under Vibration, *Sep. Purif. Technol.*, 2022, **283**, 120159.

17 Z. Wu, T. Xu, L. Ruan, J. Guan, S. Huang, X. Dong, H. Li and Y. Jia, Strong Tribocatalytic Nitrogen Fixation of Graphite Carbon Nitride g-C_3N_4 through Harvesting Friction Energy, *Nanomaterials*, 2022, **12**, 1981.

18 Y. Feng, L. Ling, Y. Wang, Z. Xu, F. Cao, H. Li and Z. Bian, Engineering Spherical Lead Zirconate Titanate to Explore the Essence of Piezo-catalysis, *Nano Energy*, 2017, **40**, 481–486.

19 J. Wu, Q. Xu, E. Lin, B. Yuan, N. Qin, S. K. Thatikonda and D. Bao, Insights into the Role of Ferroelectric Polarization in Piezocatalysis of Nanocrystalline $BaTiO_3$, *ACS Appl. Mater. Interfaces*, 2018, **10**, 17842–17849.

20 H. Y. Zhang, J. D. Dai and C. M. Liu, The Fabrication, Microstructure, Photo-catalysis and Piezo-catalysis of Layered TiO_2-MoS_2, *Mater. Res. Express*, 2018, **6**, 025025.

21 D. Liu, Y. Song, Z. Xin, G. Liu, C. Jin and F. Shan, High-piezocatalytic Performance of Eco-friendly $(Bi_{1/2}Na_{1/2})TiO_3$-based Nanofibers by Electrospinning, *Nano Energy*, 2019, **65**, 104024.

22 F. Mushtaq, X. Chen, M. Hoop, H. Torlakcik, E. Pellicer, J. Sort, C. Gattinoni, B. J. Nelson and S. Pané, Piezoelectrically Enhanced Photocatalysis with $BiFeO_3$ Nanostructures for Efficient Water Remediation, *iScience*, 2018, **4**, 236–246.

23 H. Lei, H. Zhang, Y. Zou, X. Dong, Y. Jia and F. Wang, Synergetic Photocatalysis/Piezocatalysis of Bismuth Oxybromide for Degradation of Organic Pollutants, *J. Alloys Compd.*, 2019, **809**, 151840.

24 K. D. Rajan, P. P. Gotipamul, S. Khanna, S. Chidambaram and M. Rathinam, Piezo-photocatalytic Effect of $NaNbO_3$ Interconnected Nanoparticles Decorated $CuBi_2O_4$ Nanocuboids, *Mater. Lett.*, 2021, **296**, 129902.

25 R. P. Ummer, S. Perumbilavil, J. Jose, S. Thomas, P. Gopinath and N. Kalarikkal, Exploring the Optical Limiting, Photocatalytic and Antibacterial Properties of the $BiFeO_3$-$NaNbO_3$ Nanocomposite System, *RSC Adv.*, 2021, **11**, 8450–8458.

26 S. Kumar, T. Malik, D. Sharma and A. K. Ganguli, $NaNbO_3$/MoS_2 and $NaNbO_3$/$BiVO_4$ Core−shell Nanostructures for

Photoelectrochemical Hydrogen Generation, *ACS Appl. Nano Mater.*, 2019, **2**, 2651–2662.

27 S. Singh and N. Khare, Coupling of Piezoelectric, Semiconducting and Photoexcitation Properties in NaNbO$_3$ Nanostructures for Controlling Electrical Transport: Realizing an Efficient Piezo-photoanode and Piezo-photocatalyst, *Nano Energy*, 2017, **38**, 335–341.

28 D. Yu, Z. Liu, J. Zhang, S. Li, Z. Zhao, L. Zhu, W. Liu, Y. Lin, H. Liu and Z. Zhang, Enhanced Catalytic Performance by Multi-field Coupling in KNbO$_3$ Nanostructures: Piezo-photocatalytic and Ferro-photoelectrochemical Effects, *Nano Energy*, 2019, **58**, 695–705.

29 H. You, X. Ma, Z. Wu, L. Fei, X. Chen, J. Yang, Y. Liu, Y. Jia, H. Li, F. Wang and H. Huang, Piezoelectrically/Pyroelectrically-driven Vibration/Cold-hot Energy Harvesting for Mechano-/pyro- bi-catalytic Dye Decomposition of NaNbO$_3$ Nanofibers, *Nano Energy*, 2018, **52**, 351–359.

30 L. Wang, W. Ren, P. Shi and X. Wu, Cobalt Doping Effects on Structures and Electrical Properties of Lead-free Ferroelectric K$_{0.5}$Na$_{0.5}$NbO$_3$ Films, *J. Alloys Compd.*, 2014, **608**, 202–206.

31 P. Kumari, M. Lal, S. Kumar, R. Rai, A. Singh, D. V. Karpinsky and I. Bdikin, Comprehensive Investigation of Structural, Dielectric and Local Piezoelectric Properties of KNN Ceramics, *J. Adv. Dielectr.*, 2019, **09**, 1950016.

32 Y. Saito, H. Takao, T. Tani, T. Nonoyama, K. Takatori, T. Homma, T. Nagaya and M. Nakamura, Lead-free Piezoceramics, *Nature*, 2004, **432**, 84–87.

33 Y. Sun, F. Guo, J. Chen and S. Zhao, Improved Ferroelectric and Photovoltaic Properties of BiMnO$_3$ Modified Lead-free K$_{0.5}$Na$_{0.5}$NbO$_3$ Solid-solution Films, *Appl. Phys. Lett.*, 2017, **111**, 253901.

34 S. Bairagi and S. W. Ali, Effects of Surface Modification on Electrical Properties of KNN Nanorod-incorporated PVDF Composites, *J. Mater. Sci.*, 2019, **54**, 11462–11484.

35 D. Zhou, N. Wang, T. Yang, L. Wang, X. Cao and Z. L. Wang, A Piezoelectric Nanogenerator Promotes Highly Stretchable and Self-chargeable Supercapacitors, *Mater. Horiz.*, 2020, **7**, 2158–2167.

36 Q.-T. Xue, Z. Wang, H. Tian, Y. Huan, Q.-Y. Xie, Y. Yang, D. Xie, C. Li, Y. Shu, X.-H. Wang and T.-L. Ren, A Record Flexible Piezoelectric KNN Ultrafine-grained Nanopowder-based Nanogenerator, *AIP Adv.*, 2015, **5**, 017102.

37 M. Xia, C. Luo, X. Su, Y. Li, P. Li, J. Hu, G. Li, H. Jiang and W. Zhang, KNN/PDMS/C-based Lead-free Piezoelectric Composite Film for Flexible Nanogenerator, *J. Mater. Sci.: Mater. Electron.*, 2019, **30**, 7558–7566.

38 D. Kumar, S. Sharma and N. Khare, Piezo-phototronic and Plasmonic Effect Coupled Ag-NaNbO$_3$ Nanocomposite for Enhanced Photocatalytic and Photoelectrochemical Water Splitting Activity, *Renewable Energy*, 2021, **163**, 1569–1579.

39 Y.-H. Si, Y.-Y. Li, Y. Xia, S.-K. Shang, X.-B. Xiong, X.-R. Zeng and J. Zhou, Fabrication of Novel ZIF-8@BiVO$_4$ Composite with Enhanced Photocatalytic Performance, *Crystals*, 2018, **8**, 432.

40 J. Yu, Z. Chen, L. Zeng, Y. Ma, Z. Feng, Y. Wu, H. Lin, L. Zhao and Y. He, Synthesis of cCarbon-doped KNbO$_3$ Photocatalyst with Excellent Performance for Photocatalytic Hydrogen Production, *Sol. Energy Mater. Sol. Cells*, 2018, **179**, 45–56.

41 R. Guo, Y. Guo, H. Duan, H. Li and H. Liu, Synthesis of Orthorhombic Perovskite-Type ZnSnO$_3$ Single-Crystal Nanoplates and Their Application in Energy Harvesting, *ACS Appl. Mater. Interfaces*, 2017, **9**, 8271–8279.

42 F. Wang, Y.-W. Mai, D. Wang, R. Ding and W. Shi, High Quality Barium Titanate Nanofibers for Flexible Piezoelectric Device Applications, *Sens. Actuators, A*, 2015, **233**, 195–201.

43 X. Xu, L. Xiao, Z. Wu, Y. Jia, X. Ye, F. Wang, B. Yuan, Y. Yu, H. Huang and G. Zou, Harvesting Vibration Energy to Piezo-catalytically Generate Hydrogen through Bi$_2$WO$_6$ Layered-perovskite, *Nano Energy*, 2020, **78**, 105351.

44 A. Biswas, S. Saha and N. R. Jana, ZnSnO$_3$ Nanoparticle-Based Piezocatalysts for Ultrasound-Assisted Degradation of Organic Pollutants, *ACS Appl. Nano Mater.*, 2019, **2**, 1120–1128.

45 S. Wang, Z. Wu, J. Chen, J. Ma, J. Ying, S. Cui, S. Yu, Y. Hu, J. Zhao and Y. Jia, Lead-free Sodium Niobate Nanowires with Strong Piezo-catalysis for Dye Wastewater Degradation, *Ceram. Int.*, 2019, **45**, 11703–11708.

46 G. Li, T. Kako, D. Wang, Z. Zou and J. Ye, Synthesis and Enhanced Photocatalytic Activity of NaNbO$_3$ Prepared by Hydrothermal and Polymerized Complex Methods, *J. Phys. Chem. Solids*, 2008, **69**, 2487–2491.